CrossMark

Theoretical analysis and model test for rainfall-induced shallow landslides in the red-bed area of Sichuan

L. Z. Wu[1] · L. M. Zhang[2] · Y. Zhou[1] · Q. Xu[1] · B. Yu[1] · G. G. Liu[1] ·
L. Y. Bai[1]

Abstract Heavy rainfall is a key cause of shallow landslides in red-bed terrains with steep topography and residual soils of degradable strength. In this study, laboratory model tests were carried out to examine the characteristics of rainfall infiltration, deformation, and failures of slopes in the red-bed area of Sichuan. The hydrological response and deformation of the slope soil during rainfall are addressed. Based on a modified Green–Ampt infiltration model, ponding along the bedrock surface is incorporated. A physically based model for shallow landslides caused by rainfall is developed. The theoretical analysis and the model test results indicate that the slope failures are related to erosion in the shallow soil layer and rainwater infiltration, particularly along preferential seepage channels. The process of rainfall-induced shallow landslides can be separated into three stages: erosion at the slope toe, tension crack formation at the slope crest, and shallow sliding. When initial underground water level is located at the bedrock surface or the preferential seepage flow quickly reaches the bedrock surface, it is easier for the soil slopes to slide along the bedrock surface than along the wetting front.

Keywords Shallow landslide · Rainfall infiltration · Model test · Stability analysis

Introduction

Rainfall-induced landslides can cause loss of human lives and considerable damage to infrastructure, and demand greater attention as weather conditions become more extreme because of climate change. Rainfall-induced geological disasters including residual soil slope failures commonly occur because of rainfall infiltration, particularly in tropical and subtropical areas (Rahardjo et al. 1995; Fourie 1996; Cevasco et al. 2014; Zhang et al. 2014). Rainfall-induced slope failure is produced by an increase in pore-water pressure, a rise in unit weight of the soil mass, and hydrodynamic forces during or shortly after a period of intense rainfall (Muntohar and Liao 2009, 2010; Zhang et al. 2011; White and Singham 2012). An increase in the pore-water pressure can reduce the effective stress of the soil mass and thereby weaken the shear strength. In an unsaturated soil, negative pore-water pressures increase the shear strength of the soil mass and thus help maintain the stability of unsaturated soil slopes (Fredlund and Rahardjo 1993).

Rainfall-induced slope failures have been examined by laboratory or field experiments, numerical methods, and field observations (Iverson 2000; Chen et al. 2005; Hong et al. 2005). Laboratory or field experiments were carried out to examine infiltration mechanisms and rainfall-induced slope failures (e.g., Lee et al. 2011; Wu et al. 2015, 2017a). Many numerical studies have been performed to investigate the hydraulic response of unsaturated slopes to rainfall infiltration and their associated stability (Ng and Shi 1998; Iverson 2000; Cai and Ugai 2004;

✉ Q. Xu
  xq@cdut.edu.cn

1 State Key Laboratory of Geohazard Prevention and Geoenvironment Protection, Chengdu University of Technology, Chengdu 610059, Sichuan, People's Republic of China

2 Department of Civil and Environmental Engineering, The Hong Kong University of Science and Technology, Clear Water Bay, Kowloon, Hong Kong, People's Republic of China

🖄 Springer

Zhang et al. 2005; Garcia et al. 2011; Li et al. 2013; Tsai and Chiang 2013; Ali et al. 2014; Chen and Zhang 2014; Gao et al. 2015; Wu et al. 2016, 2017b). Slope monitoring systems help collect data and analyze rainfall-induced landslide hazards (Muntohar and Liao 2009, 2010). Hydrologic models based on the Richards equation (1931) have been developed to successfully simulate transient pore-water pressures and analyze slope failures.

Shallow rainfall-induced landslides are characterized as failures that occur along a plane parallel to the ground surface. Many infinite slope models have been used to assess slope stability under conditions of heavy rainfall (Cho and Lee 2001, 2002; Tsai and Yang 2006; Tsai 2008; White and Singham 2012; Li et al. 2013; Zhan et al. 2013). These models are based on one assumption that each slice of an infinite slope receives the same amount of rainfall (Collins and Znidarcic 2004), and that the time required for infiltration normal to the slope is much less than that required for lateral flows parallel to the slope. The wetting front propagates perpendicular to the slope (White and Singham 2012) and the failure depth is small compared with the length of the failing soil mass (Ali et al. 2014). The validity of these assumptions has been checked against predictions of two-dimensional numerical models, with the conclusion that an infinite slope approximation may be used to assess slope failures caused by rainfall infiltration (Li et al. 2013).

Factors that affect the stability of a soil slope subjected to rainfall infiltration include rainfall characteristics (duration, intensity, and pattern), saturated hydraulic conductivity of the soil, slope geometry, initial soil moisture conditions, and boundary conditions (Ali et al. 2014). The boundary conditions in the aforementioned type of landslides involve an impermeable boundary (Ng and Shi 1998; White and Singham 2012; Li et al. 2013) or a drained boundary (e.g. Collins and Znidarcic 2004; Lu and Gout 2008; Tsai 2011).

Both empirical and physically based methods have been used to examine rainfall-induced slope failures. The time of a landslide is commonly predicted based on rainfall intensity and/or accumulated rainfall. Critical rainfall and duration are widely used to define a critical condition for triggering landslides. However, such empirical equations vary by region. Therefore, their application is limited to specific areas (Muntohar and Liao 2010).

Red strata are widespread in the Sichuan Basin and the Three Gorges Reservoir area, China, which are often called "landslide-prone strata" (Jian et al. 2009; Huang 2012). Red strata are continental sedimentary rocks composed of alternating red mudstone and sandstone (Zhang et al. 2015). The dip angle in the red-stratum regions generally ranges from 3 to 5° (Fan et al. 2009). Three key causes inducing retrogressive landslides in gently dipping red

strata are intensive rainfall, incompetent beds, and unloading cracks at the crest of the slopes (Jian et al. 2009). The interbedding layer of sandstone and mudstone is also a significant factor affecting the failure of red-strata slopes (Miao et al. 2014), which induced some typical landslides, including landslide groups in Wanzhou (Jian et al. 2009), the Tiantai landslide (Huang 2012), the Qianjiangping landslide (Tang et al. 2017), and the Sanxicun landslide (Yin et al. 2016; Wu et al. 2017c). The hydrostatic pressure at the scarp together with the uplift action along the sliding plane promote the occurrence of landslides. The slow-inclination landslide development in the bed-strata area is closely related to the properties of the interlayer or weak surface in the red-bed area.

The objective of the present work is to develop a physically based model for shallow landslides in red-bed regions. Based on a modified Green–Ampt infiltration model, ponding at the bedrock surface of the slope is examined. Laboratory model tests were conducted to discover the characteristics of rainfall infiltration, deformation, and failure of a slope. The hydrological response of red-bed slopes and the advancement of the wetting front are discussed.

Geographic and geologic setting

The extraordinary "9–16" rainstorm in 2011, with a rainfall intensity of 250.4 mm/day, induced thousands of shallow landslides in Nanjiang County, Sichuan Province, which is in the southwest red-bed area (Fig. 1). Because of unique engineering properties, the red beds are sliding-prone strata in which geological hazards are common. The small dip angle in the red-bed area is much less than the interface internal frictional angle between bedding planes, which is commonly greater than 30° (Zhang et al. 2015). Such gently inclined slopes in the red-bed region are unlikely to fail along the bedding planes. However, many storm-induced landslides occur in the red-strata region every year. These rainfall-induced slope failures often slide along the bedding planes.

Red beds are typical sedimentary strata with red color, and are widely distributed across China (Fig. 1a). Especially in the southwest region (V), Sichuan Basin, and its surrounding areas, Mesozoic red beds are very extensive, with a total area of approximately 260×10^3 km^2. This is known as the "red basin". Accordingly, the red beds of Sichuan are the most representative of red strata. In the northwest region (IV), red beds are covered with quaternary loess, and landslides often move along the loess and red strata interface. In the east region (I, II, III), red beds are found in various small basins of Cretaceous and Paleogene age. The western region (VI) is dominated by Cenozoic red beds, and oceanic red beds of the Qinghai

Fig. 1 Location of study region. **a** Distribution of red beds in China. **b** Landslide shape: *1* Quaternary eluvium and deluvial; *2* landslide deposit; *3* sliding boundary; *4* deformation zone; *5* sliding direction; *6* scarp; *7* gully; *8* road. **c** Overburden layer. **d** Trailing of landslide. **e** Bedrock
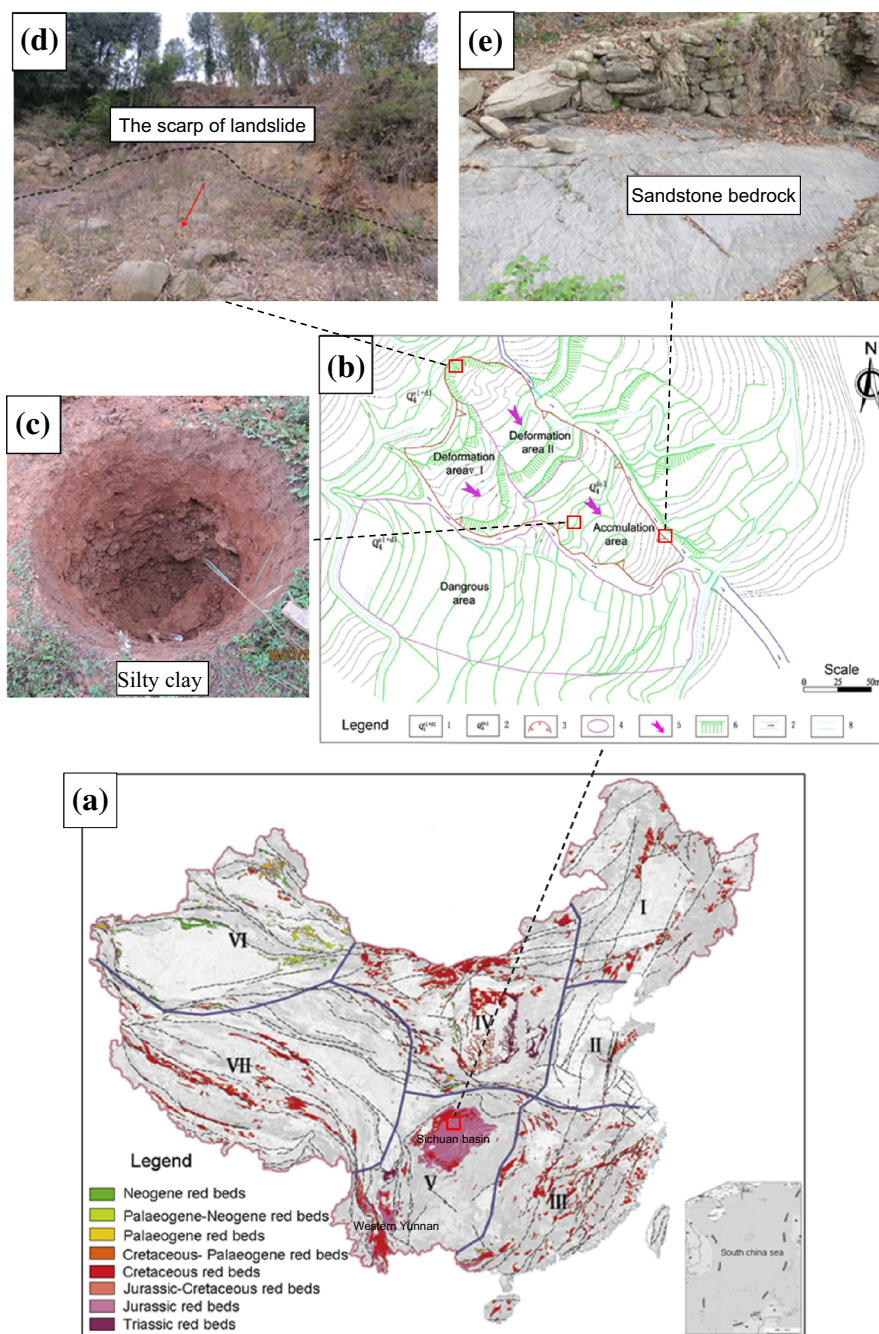
Tibet Plateau (VII) are largely coincident with major fault zones.

In the southwest region (V in Fig. 1a), the types of red beds are unique. The beds in the central Sichuan Basin are usually horizontal, with small-size accumulation of landslides. With strong tectonic and joint developments, geologic hazards including collapses and landslides are frequently caused by heavy rainfall. The study area, which is in the northern part of the Sichuan Basin red beds, shows gently inclined strata. Landslides in this area occur along the bedrock surface or the interface between two rock strata.

Landforms in the study region represent middle and low mountain landscapes, and the main rock structure is gentle. The red-bed rock mainly consists of Jurassic sandstone, with a dip angle of 15°–22°. The overburden is composed of slope deposits 1–5 m in thickness. The average annual temperature is 16 °C (1971–2000 average), and the annual rainfall is 1150 mm. The groundwater is mainly in the overburden layer, and controlled by rainfall.

The Gufenping landslide (Fig. 1b) is an example of small shallow landslides in the red-bed region. Its coordinates are 106°46′33.30″E, 32°21′46.45″N. The elevation of

the landslide front is 630 m, with a width of 50 m. The scarp elevation is 731 m and the scar width is 120 m. The elevation difference between the front and the scarp is 101 m. The landslide is 250 m in length, 131° in slip direction, 7.5 m in average thickness, and 5.81×10^4 m^3 in total volume. The strata in the landslide area were classified into two layers, a silty clay layer (Fig. 1c) and the sandstone bedrock (Fig. 1e).

Theoretical modelling of rainfall-induced shallow landslides

Modified Green–Ampt rainfall infiltration model

A shallow silty clay layer is widespread in the study area. Rainfall intensity was assumed to be greater than the infiltration rate of the silty clay, for which the coefficient of permeability at full saturation is very low. During rainfall, the slope surface becomes saturated quickly. Therefore, the infiltration into a silty clay slope can be considered a ponding infiltration process. The Green–Ampt model is a simplified representation of the infiltration process. The model assumes that a wetting front is present in the soil profile, and that the front separates the profile into an upper saturated zone and a lower unsaturated zone, where the water content is kept at the initial condition. The original Green–Ampt model was used to analyze the one-dimensional infiltration rather than the slope infiltration. The slope infiltration can be analyzed using an appropriately modified and simplified Green–Ampt model (Muntohar and Liao 2009, 2010). Based on Darcy's law, the infiltration rate in a slope caused by ponding at its surface is written as

$$i(t) = K_s \frac{z_f^* \cos \alpha + s_f + H}{z_f^*}, \tag{1}$$

where $i(t)$ is the surface infiltration rate at time t (units m/s); z_f^* is the infiltration depth perpendicular to the slope surface (m); α is the slope gradient (°); K_s is the saturated hydraulic conductivity (m/s); s_f is the suction head at the position of the wetting front (m); and H is the depth of ponding (m).

According to the principle of water balance and basic assumption of the Green–Ampt infiltration model, the cumulative infiltration capacity over time can be expressed as

$$I = \Delta\theta z_f^*, \tag{2}$$

in which $\Delta\theta$ is the difference between saturated volumetric water content θ_s and initial volumetric water content θ_i.

The infiltration rate can be given by

$$i(t) = \frac{dI}{dt} = \Delta\theta \frac{dz_f^*}{dt}. \tag{3}$$

According to Eqs. 1 and 3, one can obtain

$$\frac{dz_f^*}{dt} = \frac{K_s}{\Delta\theta} \frac{z_f^* \cos \alpha + s_f + H}{z_f^*}. \tag{4}$$

The runoff is always along the slope surface, and is hence neglected here. Therefore, the depth of ponding is shallow; $H \approx 0$ is often assumed. For shallow landslides, the negative pressure head of the soil is much larger than the infiltration depth. $h'(t)$ is the vertical infiltration depth, and $z_f^* = h'(t) \cos \alpha$. Equation 4 can be rewritten as

$$\frac{dh'(t)}{dt} = \frac{K_s s_f}{\Delta\theta \cos^2 \alpha h'(t)}. \tag{5}$$

Integrating Eq. 5 and substituting the initial condition $h'(0) = 0$, the relationship between vertical infiltration depth and time can be expressed as

$$h'(t) = \sqrt{\frac{2K_s s_f t}{\Delta\theta \cos^2 \alpha}} \tag{6}$$

Theoretical model for shallow landslides

For a shallow unsaturated soil slope, the wetting front is usually parallel to the slope surface and landslides move along the wetting front or bedrock surface, as shown in Fig. 2. In this figure, h is the thickness of the upper soil mass (m), h'' is the underground water level (m), ΔL is the unit horizontal length, which equals 1 m, σ_n is the effective normal stress at the bottom of soil slice, u_a is pore-air pressure (kPa), u_w is pore-water pressure (kPa), and τ_m is the shear stress of a soil slice. Based on the unsaturated soil shear strength (Fredlund and Rahardjo 1993) and the limit equilibrium method, the factor of safety (F_s) for the soil slope under natural conditions can be expressed as

$$F_s = \frac{\tau_f}{\tau_m} = \frac{c' + (\sigma_n - u_a) \tan \varphi' + (u_a - u_w) \tan \varphi^b}{\tau_m}, \tag{7}$$

where τ_f is the shear strength of unsaturated soil (kPa); c' is the effective cohesion (kPa); φ' is the effective angle of internal friction (°); $u_a - u_w$ is the matric suction (kPa); and φ^b is the internal friction angle associated with the soil suction (°).

Sliding surface at the wetting front

The soil mass above the wetting front is assumed to be completely saturated, i.e., the matric suction disappears completely, $u_a - u_w = 0$. The normal stress and shear stress of the soil below the wetting front can be calculated based on saturated soil mechanics. The soil stresses on a soil slice

Fig. 2 Stability analysis of an infinite slope
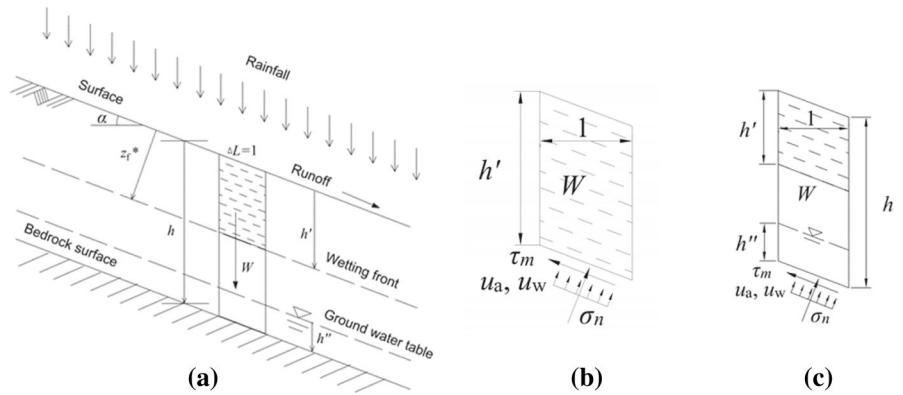
below the wetting front are shown in Fig. 2b, and the normal and shear stresses at the sliding surface are, respectively:

$$\sigma_n = \gamma_{sat} h' \cos^2 \alpha, \tag{8}$$

$$\tau_m = \gamma_{sat} h' \sin \alpha \cos \alpha, \tag{9}$$

where γ_{sat} is the saturated soil gravity density (kN m^{-3}).

When the sliding surface is along the wetting front, F_s for the slope is expressed as

$$F_s = \frac{c' + \gamma_{sat} h' \cos^2 \alpha \tan \varphi'}{\gamma_{sat} h' \sin \alpha \cos \alpha}. \tag{10}$$

Sliding surface at the bedrock surface

Without groundwater When there is no groundwater at the bedrock surface, i.e., $h'' = 0$, the normal and shear stresses on a soil slice along the sliding surface are (Fig. 2c):

$$\sigma_n = (\gamma_0 h + \Delta\gamma h') \cos^2 \alpha, \tag{11}$$

$$\tau_m = (\gamma_0 h + \Delta\gamma h') \sin \alpha \cos \alpha, \tag{12}$$

where γ_0 is the initial soil unit weight (kN m^{-3}). $\Delta\gamma$ is the difference between the saturated gravity density and the initial gravity density (kN m^{-3}).

When the wetting front has not reached the bedrock surface, $h' < h$. According to Eq. 7, when the sliding surface is along the bedrock surface, F_s for the slope can be expressed by

$$F_s = \frac{c' + (\gamma_0 h + \Delta\gamma h') \cos^2 \alpha \tan \varphi' + s_f r_w \tan \varphi^b}{(\gamma_0 h + \Delta\gamma h') \sin \alpha \cos \alpha}. \tag{13}$$

When the wetting front reaches the bedrock surface, $h' = h$; the soil is saturated and the matric suction disappears. F_s for the slope under the sliding surface along the bedrock surface can be expressed as

$$F_s = \frac{c' + \gamma_{sat} h \cos^2 \alpha \tan \varphi'}{\gamma_{sat} h \sin \alpha \cos \alpha}. \tag{14}$$

With groundwater With the presence of groundwater, the soil is saturated at the bedrock surface, whereby $u_a - u_w = 0$. According to the soil stress analysis shown in Fig. 2c, the normal and shear stresses of a unit soil slice at the sliding surface are

$$\sigma_n = [\gamma_0(h - h'') + \Delta\gamma h' + \gamma_{sat} h''] \cos^2 \alpha, \tag{15}$$

$$\tau_m = [\gamma_0(h - h'') + \Delta\gamma h' + \gamma_{sat} h''] \sin \alpha \cos \alpha. \tag{16}$$

When the sliding surface is along the bedrock surface, F_s for the slope can be expressed by

$$F_s = \frac{c' + [\gamma_0(h - h'') + \Delta\gamma h' + \gamma_{sat} h''] \cos^2 \alpha \tan \varphi'}{[\gamma_0(h - h'') + \Delta\gamma h' + \gamma_{sat} h''] \sin \alpha \cos \alpha}. \tag{17}$$

Laboratory model testing of rainfall-induced landslides

Model tests

The shallow landslides in the study area always move along the "smooth" bedrock surface. Because of this characteristic, a shallow landslide test model was created, as shown in Figs. 3 and 4. The model soil was sampled from the Gufenping landslide debris in Nanjiang. Figure 5 presents the grain-size distribution curve of the test soil. It was mainly composed of silty clay. Its soil physical parameters are listed in Table 1, and its mechanical parameters are listed in Table 2. The slope angle of the bedrock was 30°. The thickness of the sliding body was 0.15 m and the slope vertical height was 0.75 m.

The laboratory model test system included a model box, an artificial rainfall system, and a hydrologic monitoring and deformation monitoring system. Sensors were buried at various positions of the soil slope model to monitor changes in moisture content, matric suction, and pore-water pressure of the bedrock surface. A three-dimensional laser scanner with 1-mm resolution (Leica Scanstaion2,
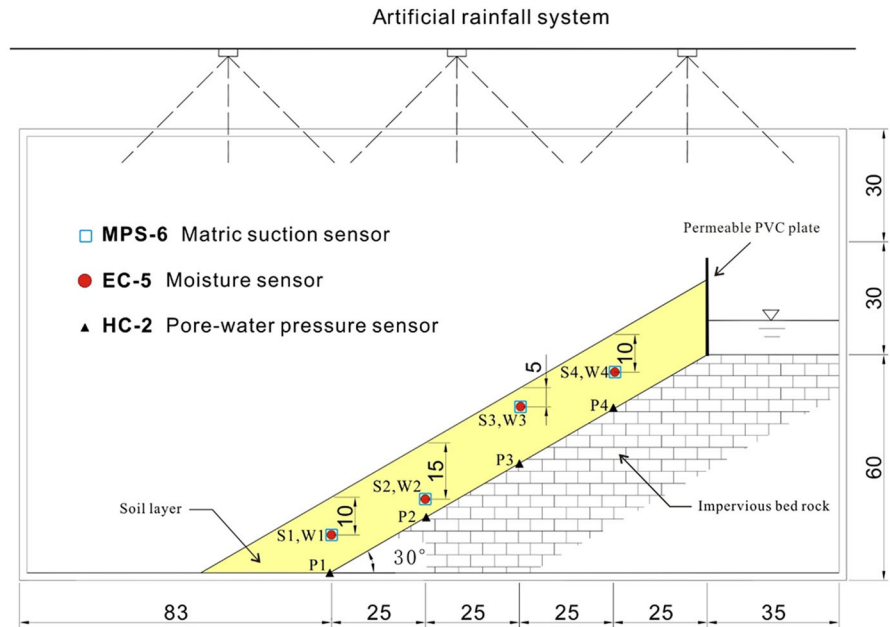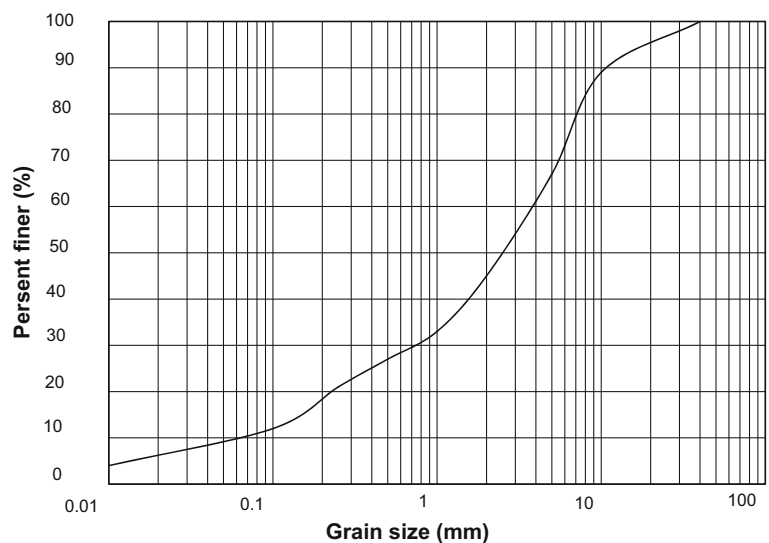
Fig. 3 Profile of the test model (unit: mm)

Fig. 4 Configuration of the test model

Fig. 5 Grain-size distribution curve of the test soil

Germany) was used to capture changes in slope surface morphology and analyze deformation and failure of the slope model during rainfall infiltration.

A model box 218 mm in length, 50 mm in width, and 120 mm in height was made for the test. Several steps were followed to prepare the model: (1) According to the test requirements, the model was divided into three layers, 5 cm thick each so as to ensure homogeneity of the slope model. The average moisture content of each soil layer was measured and calculated based on the dry density. (2) The slope model was compacted layer by layer, and the sensors were buried. (3) Cutting rings were used to obtain soil samples from the model slope, and the soil density and water content were measured. If the density was too low,

Table 1 Physical parameters of the test soil

Saturated permeability coefficient (m/s)	Saturated unit weight (kN m^{-3})	Natural unit weight (kN m^{-3})	Dry unit weight (kN m^{-3})	Liquid limit (%)	Plastic limit (%)	Plasticity index	Saturated moisture content (%)	Initial moisture content (%)
2.31×10^{-8}	19.8	15.2	13.6	46.2	21.6	24.6	47.7	4.9

Table 2 Mechanical parameters of the test soil

Effective cohesion (kPa)	Effective angle of internal friction (°)	Initial matric suction (kPa)	Compression modulus (MPa)	Compression coefficient (MPa^{-1})
11.3	12.1	110	47.7	4.9

then this soil layer required further compaction. (4) After the slope model was completed, the model was covered with plastic film for 24 h for moisture equilibrium.

Volumetric water content, matric suction, and pore-water pressure monitoring

Four EC-5 sensors (Decagon, WA, USA) were used to monitor the moisture content, four MPS-6 sensors (Decagon, WA, USA) were used to monitor the matric suction, and four HC-2 sensors (RHCT, China) were used to monitor pore-water pressures ranging from 0 to 100 kPa with an accuracy of ±0.1%. Those sensors were buried as shown in Fig. 3. The artificial rainfall intensity was 72 mm/h, and the test data were recorded every minute.

Figures 6, 7, 8 show variations in moisture content, matric suction, and pore-water pressure over the test duration. After rainfall, water first infiltrated the shallowest point, #3 (at 5 cm of depth). Its volumetric water content increased abruptly, while the matric suction decreased. With ongoing rainfall, the wetting front successively arrived at positions #1 (10 cm) and #2 (15 cm). At the same depth (points #2 and #4), the water at point #4 came from not only the slope surface but also the scarp crack. The hydrologic response at that point was more rapid than that at #2. Full sliding and failure occurred at $t = 6$ h. Under the shear action, the soil particles were displaced and the soil skeleton stress was modified. However, the soil in the sliding zone showed weak permeability. The pore-water pressures at points #1, #2, #3, and #4 suddenly increased.

Deformation and failure characteristics of the landslide

In the experiment, a shallow landslide was induced by surface erosion and water infiltration. The slope failure process could be separated into three stages, as shown in Fig. 9. These stages were as follows:
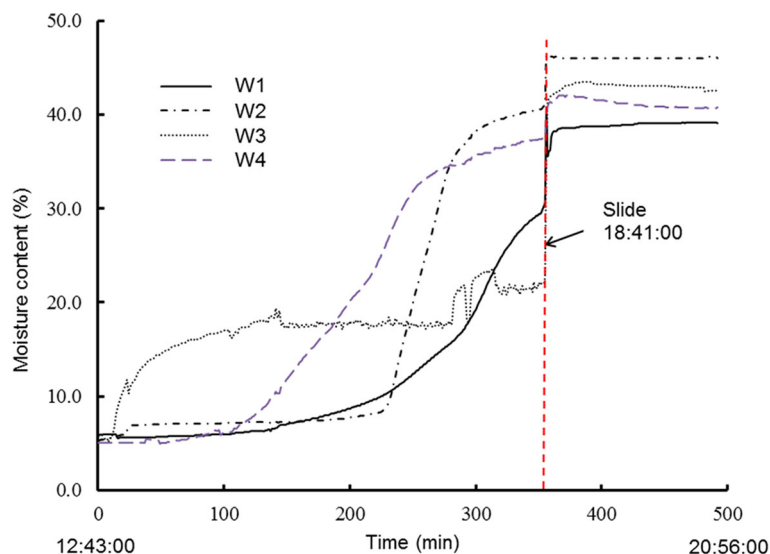
Fig. 6 Changes in moisture content with time

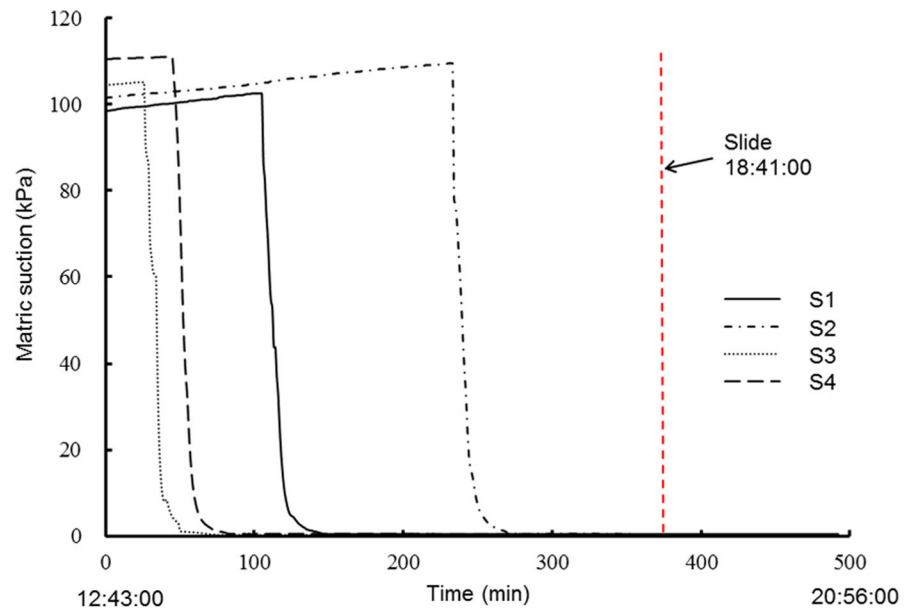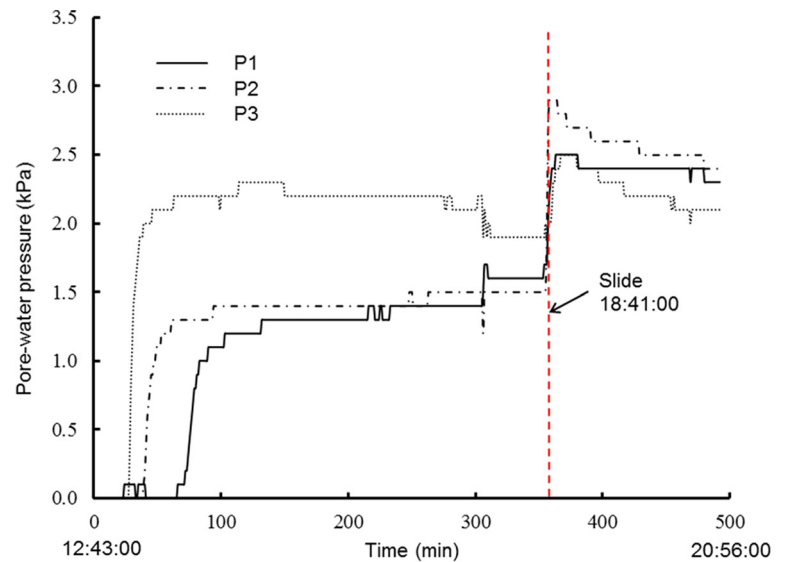**Fig. 7** Changes in matric suction with time

Fig. 8 Rising of pore-water pressure over time

(a) Stage of erosion and local failure on the slope toe. The slope surface eroded, with the erosion area gradually changing from the slope toe to the slope crest.

(b) Stage of tension cracks development on the slope crest. Owing to strong erosion at the slope toe, soil deformations developed, and small cracks formed at the slope crest. With continuing rainfall, the cracks gradually deepened and widened, generating tension cracks.

(c) Stage of shallow landslide. With increases of accumulated rainfall and rising groundwater level, the shallow part of the slope became gradually saturated, and slid along the bedrock surface. This was because the layer of the deposit moved slowly

along the interface and squeezed the bottom of the soil layer. An uplift zone occurred at the slope toe, and many tension cracks appeared in this region.

Verification of the infiltration analysis model

The relevant parameters of the modified Green–Ampt model are provided in Tables 1 and 2. Based on Eq. 6, the arrival time of the wetting front was calculated, and the accuracy of the Green–Ampt model was verified by comparing analysis results with the landslide model test.

In Table 3, the results from the modified Green–Ampt model agree well with those of the model test. The

Fig. 9 Evolution of a shallow landslide: **a** initial state; **b** erosion and local failure at the slope toe; **c** tension cracks on the slope crest; **d** shallow landslide


(a)

(b)

(c)

(d)
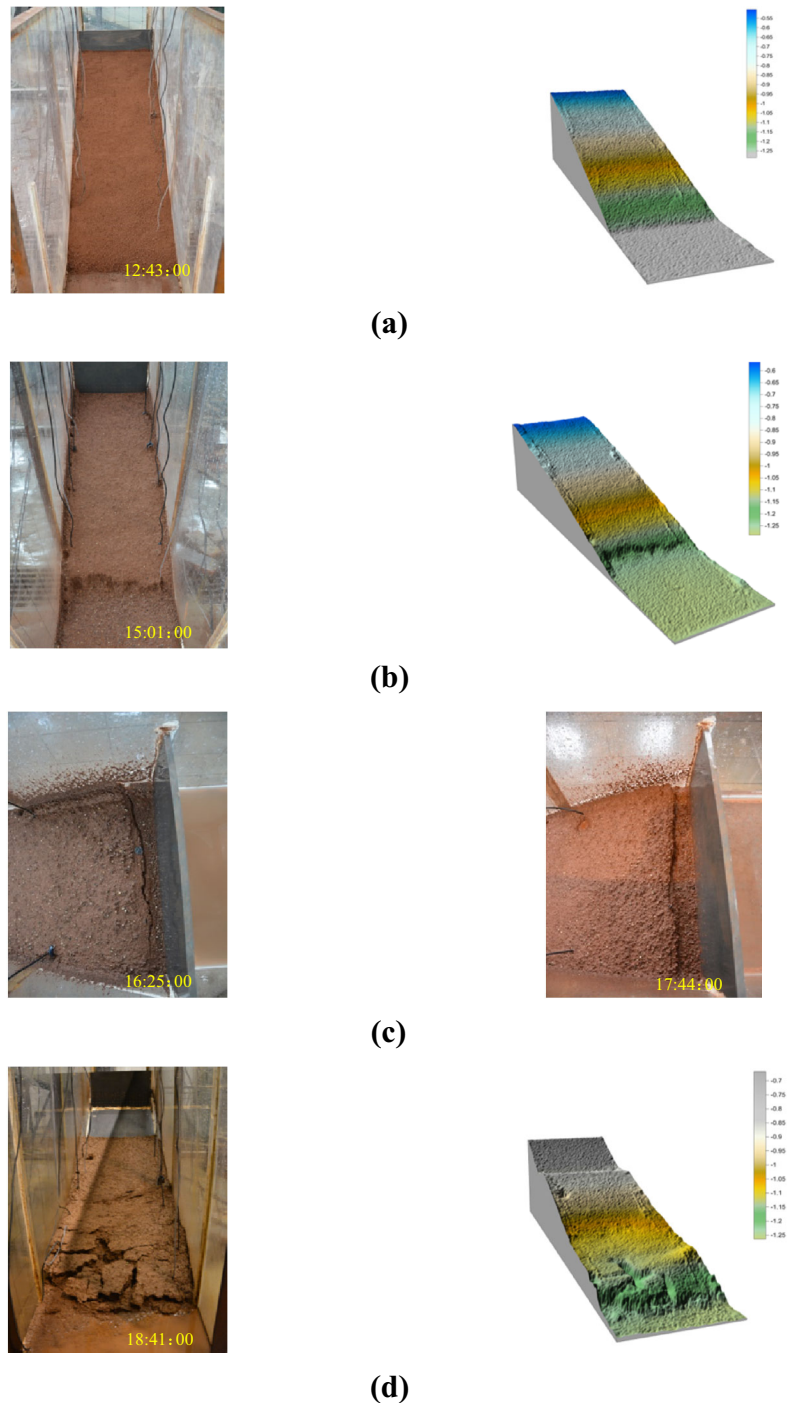
calculated value slightly lagged behind the monitoring value. The theoretical model indicates that the wetting front moves downward by 5 cm in 26.55 min, which is close to the monitoring value of 25 min. The discrepancy may be related to the assumption in the theoretical model that the infiltration rate of the slope equals the saturated coefficient of permeability at full saturation. However, before the ponding stage, the actual infiltration rate is larger than the saturated coefficient of permeability. When the wetting front depth was 10 cm, the difference between the calculated and experimental monitoring values was 1.19 min. However, when the wetting front depth was 15 cm, the experimental monitoring result was 5.93 min faster than the calculated result. This is because point S2 was near the bedrock. The rainwater could infiltrate the soil through the scarp crack and migrate along the bedrock surface, raising the underground water level. This caused the monitoring response time to be shorter than that of the

Table 3 Comparison between results of improved infiltration model and monitored data

Sensor	Depth (cm)	Calculated arrival time of wetting front (min)	Monitored arrival time of wetting front (min)	Difference (min)
S3	5	26.6	25	1.6
S1	10	106.2	105	1.2
S2	15	238.9	233	5.9
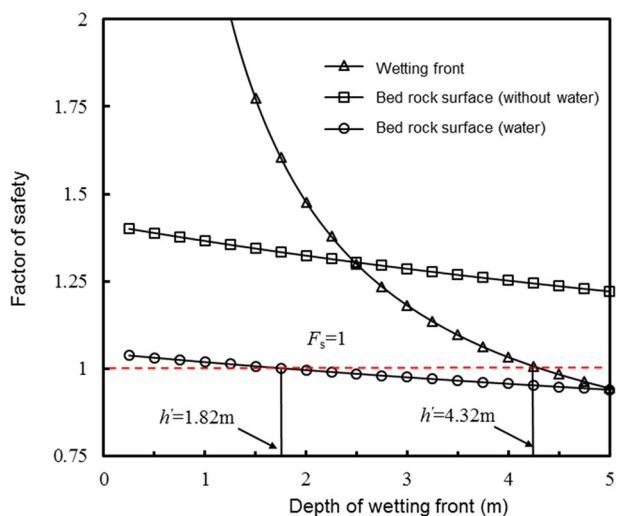
Fig. 10 Variation of factor of safety with depth of wetting front

calculation model. Therefore, the modified Green–Ampt model can be applied to study the rainfall infiltration in such a red-bed slope.

Comparative analysis of the shallow landslide model

The shallow soil landslides in the red-bed area of Nanjiang usually have thicknesses of 1–5 m and slope angles of 10°–30°. Therefore, an infinite shallow soil slope model with a slope angle of 20° was assumed for comparison analysis. The thickness of the top slope soil layer is 5 m, and the lower part is an impermeable bedrock layer. The underground water level, parallel to the bedrock surface, has a depth of 0.25 m. The initial soil suction head is 5 m. The effective cohesion is 11.3 kPa and the effective friction angle is 12.1° according to our direct shear tests, which were controlled at a displacement rate of 0.06 mm/min according to ASTM D 5321 (ASTM D 2003). The internal friction angle related to the soil suction was 10°. Based on Eqs. 10, 13, and 17, the F_s values are obtained for sliding surfaces along the wetting front and along the bedrock surface (Fig. 10).

With the downward movement of the wetting front, the soil unit weight of the slope gradually increased, and the F_s of the slope was gradually reduced. The F_s for the sliding surface at the wetting front decreased exponentially with infiltration depth, while the F_s of the sliding surface in the bedrock surface decreased slowly. When the depth of the wetting front was 1.82 m and the sliding surface was at the bedrock surface (groundwater condition), the F_s of the slope was 1. However, the F_s of the slope for the sliding surface at the wetting front was 1.56. This indicates that the slope will slide along the bedrock surface if rainwater infiltrates to a depth of 1.82 m.

Therefore, the slope will become unstable if the initial groundwater is at the bedrock surface or if the rainwater infiltrates the bedrock surface along preferential channels. That is, the soil slope can fail along the bedrock surface, even if the wetting front does not reach that surface.

Conclusions

Through a laboratory model test and theoretical analysis of the rainfall-induced shallow soil landslides in the red-bed region in Sichuan, the following conclusions can be drawn:

1. Rainfall infiltration can reduce the strength of the soil due to loss of matric suction in an unsaturated soil slope. Laboratory test results indicate that rainwater surface erosion influences the integrity of the slope. The shallow soil slope deformation caused by rainfall infiltration is related to rainwater surface erosion. The slope deformation increases gradually with time. The failure process can be separated into three stages: erosion and local failure at the slope toe, tension crack formation at the slope crest, and shallow sliding.

2. When there is no preferential flow channel and the initial groundwater table is very low, the sliding surface in the red-bed regions is along the wetting front. Based on the modified Green–Ampt infiltration model, the sliding surface at the wetting front and the bedrock surface were considered in developing a model for shallow landslides caused by rainfall infiltration. However, slope failure occurs earlier along the bedrock surface than along the wetting front if the initial groundwater level is at the bedrock surface or the rainwater moves along the bedrock surface.

References

Ali A, Huang JS, Lyamin AV, Sloan SW, Cassidy MJ (2014) Boundary effects of rainfall-induced landslides. Comput Geotech 61:341–354

ASTM D 3080-98 (2003) Standard test method for direct shear test of soils under consolidated drained conditions Annual Book of ASTM Standards. American Society For Testing and Materials, West Conshohocken, pp 347–352

Cai F, Ugai K (2004) Numerical analysis of rainfall effects on slope stability. Int J Geomech 4(2):69–78

Cevasco A, Pepe G, Brandolini P (2014) The influences of geological and land use settings on shallow landslides triggered by an intense rainfall event in a coastal terraced environment. Bull Eng Geol Environ 73:859–875

Chen HX, Zhang LM (2014) A physically-based distributed cell model for predicting regional rainfall-induced slope failures. Eng Geol 176:79–92

Chen CY, Chen TC, Yu WH, Lin SC (2005) Analysis of time-varying rainfall infiltration induced landslide. Environ Geol 48:466–479

Cho SE, Lee SR (2001) Instability of unsaturated soil slopes due to infiltration. Comput Geotech 28:185–208

Cho SE, Lee SR (2002) Evaluation of surficial stability for homogeneous slopes considering rainfall characteristics. J Geotech Geoenviron 128(9):756–763

Collins BD, Znidarcic D (2004) Stability analyses of rainfall induced landslides. J Geotech Geoenviron 130(4):362–372

Fan XM, Xu Q, Zhang ZY, Meng DS, Tang R (2009) The genetic mechanism of a translational landslide. Bull Eng Geol Environ 68(2):231–244

Fourie AB (1996) Predicting rainfall-induced slope instability. Proc ICE Geotech Eng 119(4):211–218

Fredlund DG, Rahardjo H (1993) Soil mechanics for unsaturated soils. Wiley, New York

Gao L, Zhang LM, Chen HX (2015) Likely scenarios of natural terrain shallow slope failures on Hong Kong Island under extreme storms. Nat Hazards Rev. doi:10.1061/(ASCE)NH.1527-6996.0000207 (B4015001)

Garcia E, Oka F, Kimoto S (2011) Numerical analysis of a one-dimensional infiltration problem in unsaturated soil by a seepage–deformation coupled method. Int J Numer Anal Methods Geomech 35(5):544–568

Hong Y, Hiura H, Shino K, Sassa K, Fukuoka H (2005) Quantitative assessment on the influence of heavy rainfall on the crystalline schist landslide by monitoring system-case study on Zentoku landslide Japan. Landslides 2:31–41

Huang RQ (2012) Mechanisms of large-scale landslides in China. Bull Eng Geol Environ 71(1):161–170

Iverson RM (2000) Landslide triggering by rain infiltration. Water Resour Res 36(7):1897–1910

Jian WX, Wang ZJ, Yin KL (2009) Mechanism of the Anlesi landslide in the Three Gorges Reservoir, China. Eng Geol 108(1–2):86–95

Lee LM, Kassim A, Gofar N (2011) Performances of two instrumented laboratory models for the study of rainfall infiltration into unsaturated soils. Eng Geol 117(1–2):78–89

Li WC, Lee LM, Cai H, Li HJ, Dai FC, Wang ML (2013) Combined roles of saturated permeability and rainfall characteristics on surficial failure of homogeneous soil slope. Eng Geol 153:105–113

Lu N, Gout JW (2008) Infinite slope stability under steady unsaturated seepage conditions. Water Resour Res 44(11):W11404

Miao HB, Wang GH, Yin KL, Kamai T, Li YY (2014) Mechanism of the slow-moving landslides in Jurassic red-strata in the Three Gorges Reservoir, China. Eng Geol 171:59–69

Muntohar AS, Liao HJ (2009) Analysis of rainfall-induced infinite slope failure during typhoon using a hydrological–geotechnical model. Environ Geol 56:1145–1159

Muntohar AS, Liao HJ (2010) Rainfall infiltration: infinite slope model for landslides triggering by rainstorm. Nat Hazards 54:967–984

Ng CWW, Shi Q (1998) A numerical investigation of the stability of unsaturated soil slopes subjected to transient seepage. Comput Geotech 22(1):1–28

Rahardjo H, Lim TT, Chang MF, Fredlund DG (1995) Shear-strength characteristics of a residual soil. Can Geotech J 32(1):60–77

Richards LA (1931) Capillary conduction of liquids through porous mediums. Physics 1(5):318–333

Tang HM, Yong R, Ez Eldin MAM (2017) Stability analysis of stratified rock slopes with spatially variable strength parameters: the case of Qianjiangping landslide. Bull Eng Geol Environ. 76(3):839–853

Tsai TL (2008) The influence of rainstorm pattern on shallow landslide. J Environ Geol 53(7):1563–1569

Tsai TL (2011) Influences of soil water characteristic curve on rainfall-induced shallow landslides. Environ Earth Sci 64(2):449–459

Tsai TL, Chiang SJ (2013) Modeling of layered infinite slope failure triggered by rainfall. Environ Earth Sci 68(5):1429–1434

Tsai TL, Yang JC (2006) Modeling of rainfall-triggered shallow landslide. Environ Geol 50(4):525–534

White JA, Singham DI (2012) Slope stability assessment using stochastic rainfall simulation. Procedia Comput Sci 9:699–706

Wu LZ, Huang RQ, Xu Q, Zhang LM, Li HL (2015) Analysis of physical testing of rainfall-induced soil slope failures. Environ Earth Sci 73(12):8519–8531

Wu LZ, Liu GG, Wang LC, Zhang LM, Li BE, Li B (2016) Numerical analysis of 1D coupled infiltration and deformation in layered unsaturated porous medium. Environ Earth Sci 75:761. doi:10.1007/s12665-016-5579-4

Wu LZ, Zhou Y, Sun P, Shi JS, Liu GG, Bai LY (2017a) Laboratory characterization of rainfall-induced loess slope failure. Catena 150:1–8

Wu LZ, Zhang LM, Zhou Y, Li B E (2017b) Analysis of multi-phase coupled seepage and stability in anisotropic slopes under rainfall condition. Environ Earth Sci 76(14):469

Wu LZ, Shi JS, Xu Q (2017c) The rainfall-induced Wulipo rockslide, China: a modified model for rockslide initiation. Environ Earth Sci 76(14):497

Yin YP, Cheng YL, Liang JT, Wang WP (2016) Heavy-rainfall-induced catastrophic rockslide-debris flow at Sanxicun, Dujiangyan, after the Wenchuan Ms 8.0 earthquake. Landslides 13(1):9–23

Zhan TLT, Jia GW, Chen YM, Fredlund DG, Li H (2013) An analytical solution for rainfall infiltration into an unsaturated infinite slope and its application to slope stability analysis. Int J Numer Anal Methods Geomech 37(12):1737–1760

Zhang LL, Zhang LM, Tang WH (2005) Rainfall-induced slope failure considering variability of soil properties. Geotechnique 55(2):183–188

Zhang LL, Zhang J, Zhang LM, Tang WH (2011) Stability analysis of rainfall-induced slope failures: a review. Proc ICE Geotech Eng 164(5):299–316

Zhang S, Zhang LM, Glade T (2014) Characteristics of earthquake- and rain-induced landslides near the epicenter of Wenchuan Earthquake. Eng Geol 175:58–73

Zhang M, Yin Y, Huang BL (2015) Mechanisms of rainfall-induced landslides in gently inclined red beds in the eastern Sichuan Basin, SW China. Landslides 12(5):973–983